IEEE/ASME TRANSACTIONS ON MECHATRONICS

# Robotic Micropuncture With Preload Strategy for Retinal Vein Cannulation

Bo Hu<sup>®</sup>, Ruimin Li<sup>®</sup>, Shiyu Xu<sup>®</sup>, Rongxin Liu, Zengshuo Wang<sup>®</sup>, Mingzhu Sun<sup>®</sup>, *Member, IEEE*, and Xin Zhao<sup>®</sup>, *Member, IEEE* 

Abstract—Retinal vein cannulation (RVC) is a surgical procedure utilized in the treatment of retinal vein occlusion. During RVC, the micropuncture process encounters challenges due to unstable contact between the bent needle and the retinal vein, potentially resulting in micropuncture failure. To enhance the success rate, a robotic micropuncture procedure with preload strategy is proposed, which can increase the tissue stiffness and improve stability. First, a nonlinear viscoelastic (NV) model is developed to characterize the nonlinearity and relaxation behavior of the preload force. Subsequently, an NV model based adaptive integral terminal sliding mode controller (NAITSMC) is designed to ensure precise force tracking under tissue uncertainty and respiratory motion. The effectiveness of the robotic micropuncture is validated through in vitro experiments conducted on open-sky porcine eyes. The experimental results indicate that the NV model is more suitable for modeling the force applied to the retinal vein under various inner pressure cases. Under simulated respiratory motion, the NAITSMC demonstrates statistically reduction in error compared to the advanced sliding mode force controller. The preload strategy significantly improves the success rate, achieving a maximum rate of 90%. Furthermore, a preload force of  $40~\mu N$  is recommended, demonstrating a higher success rate while maintaining acceptable safety considerations.

Index Terms—Micromanipulation, preload strategy, retinal vein cannulation (RVC), sliding mode control, viscoelastic modeling.

Received 2 June 2025; accepted 25 July 2025. Recommended by Technical Editor A. Chemori and Senior Editor K. Oldham. This work was supported in part by the National Key R&D Program of China under Grant 2022YFB4702903, in part by the Shenzhen Science and Technology Program under Grant JCYJ20240813165501003, and in part by the Science and Technology Program of Tianjin under Grant 24ZXZSSS00420. (Corresponding authors: Mingzhu Sun; Xin Zhao.)

The authors are with the National Key Laboratory of Intelligent Tracking and Forecasting for Infectious Diseases, Engineering Research Center of Trusted Behavior Intelligence, Ministry of Education, Tianjin Key Laboratory of Intelligent Robotics, Institute of Robotics and Automatic Information System, Nankai University, Tianjin 300350, China, and also with the Institute of Intelligence Technology and Robotic Systems, Shenzhen Research Institute of Nankai University, Shenzhen 518083, China (e-mail: hubo@mail.nankai.edu.cn; Irumin@163.com; 2120220529@mail.nankai.edu.cn; 2120230484@mail.nankai.edu.cn; zengshuowang@mail.nankai.edu.cn; sunmz@nankai.edu.cn; zhaoxin@nankai.edu.cn).

Color versions of one or more figures in this article are available at https://doi.org/10.1109/TMECH.2025.3593419.

Digital Object Identifier 10.1109/TMECH.2025.3593419

#### I. INTRODUCTION

ETINAL vein occlusion (RVO) is a serious retinal disease that has the potential to lead to blindness [1], [2]. Retinal vein cannulation (RVC) represents a direct surgical intervention for RVO [3], [4]. As illustrated in Fig. 1, a microneedle is inserted to approach the retina through a scleral incision, allowing for injection following the micropuncture of the target vein [5]. This technique directly dissolves the thrombus, facilitating the restoration of blood flow. However, this surgical method is not widely adopted in clinical due to its dependence on the skill and precision of the surgeon. Currently, robotic technique is expected to mitigate these limitations. It provides flexibility and high precision during surgical procedures [6], [7]. Among these procedures, the micropuncture exhibits a relatively straightforward pattern, rendering it a promising candidate for automation. However, due to the large retina deformation during micropuncture, the successful micropuncture within a limited motion is challenging. Thus, enhancing the success rate of micropuncture remains a key objective in robotic micropuncture. The micropuncture process poses significant difficulties due to limited depth perception and the microscale of manipulation. It is essential to pierce the vein wall, while avoiding the risk of double-puncture [8]. Surgeons commonly prefer the use of a bent needle during surgical procedures [9]. The small angle between the bent needle and the retina effectively reduces the risk of puncturing the second vein wall [10], [11]. This approach is considered safer than utilizing a straight needle. However, if the angle is too small, it may lead to unstable contact, complicating the micropuncture process. In clinical practice, surgeons attempt to create a slight indentation in the retinal vein surface in advance to ensure stable contact, thus enhancing the probability of a successful subsequent micropuncture [12]. This technique can be described as a preload strategy with applications in surgical practice [13]. When the micropuncture operation is performed alongside the preload strategy, a high success rate is anticipated.

Preload strategy requires force perception to ensure the precision and safety of the contact [14]. To enhance the success rate of micropuncture, it is essential to delineate the relationship between external forces and retinal vein deformation through a mechanistic model. Among the continuum models, the solid model has been utilized in soft tissue puncture due to its intuitiveness. These models typically treat soft tissue as either a uniform elastic solid or a viscoelastic solid, employing appropriate constitutive models to characterize mechanical behavior.

1083-4435 © 2025 IEEE. All rights reserved, including rights for text and data mining, and training of artificial intelligence and similar technologies. Personal use is permitted, but republication/redistribution requires IEEE permission. See https://www.ieee.org/publications/rights/index.html for more information.

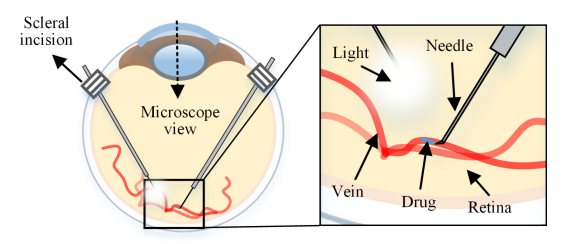


Fig. 1. Diagram of the RVC procedure.

Common structural representations include a combination of elasticity and dampers, exemplified by the Maxwell model, Kelvin–Voigt (K–V) model, the standard linear solid (SLS) model, etc. [15], [16], [17]. The SLS model is widely used because it effectively describes both the relaxation and creep behavior of soft tissue [18]. However, due to the nonlinearity exhibited by the retinal vein, the SLS model is not appropriate for this specific scenario [19]. Nonlinear force model, such as the Hunt–Crossley model, is suitable for the infinite elastic material. It is hard to account for relaxation of thin-wall retinal tissue [20]. Consequently, for robotic micropuncure, it is imperative to consider a nonlinear viscoelastic model that can accurately represent both nonlinearity and relaxation, thus facilitating surgical improvements.

In the interaction between the needle and the retinal vein, not only are there nonlinear viscoelastic properties and uncertainties associated with soft tissue, but additional motion is also induced by patient respiratory motion [21]. To establish a reliable preload strategy, it is essential to develop a precise force controller for robotic operations. A proportional-integral-derivative (PID) based force controller has been implemented to achieve compliant force control between the continuum robot and the nasal cavity model [22]. The nasal cavity model is regarded as a linear elastic material. However, the nonlinearity of retinal tissue imposes limitations on the applicability of the PID controller. To address environmental uncertainties, sliding mode control serves as an advanced force control scheme, offering significant advantages in terms of high precision and robust performance in the field of robotics. In [23], a model-free integral terminal sliding mode controller (MFITSMC) was designed to manage the complex nonlinear behavior generated by the piezoelectric actuator, thereby achieving precise force tracking. This controller utilized the time-delay estimation method to compensate for uncertainties, thereby enhancing its robustness. While the MFITSMC can minimize dynamic information, establishing the relationship between surgical instruments and the environment significantly improves the accuracy of force control. It is challenging to ensure micro-force precision when MFITSMC is directly applied to the preload strategy. In [24], an adaptive integral terminal sliding mode control (AITSMC) is proposed to achieve contact force control in tympanic membrane surgery. The AITSMC can estimate unknown parameters and switching gain, resulting in improved contact force precision. However, the AITSMC lack of full utilization of prior knowledge of soft tissues, and the assumption that the disturbance is upper bounded by unknown constant limits its ability to estimate state-dependent

disturbances in practice. Furthermore, the rapid movement of surgical instruments can cause fluctuations in microforce, which is detrimental to the stability of force control [25], [26]. Therefore, the proposed controller must address the uncertainties associated with soft tissue characteristics, respiratory disturbances, and speed constraints to achieve high-precision force control in the preload strategy.

Based on the aforementioned challenges, this article primarily focuses on improving the success rate through a preload strategy during the robotic micropuncture process. Second, a nonlinear viscoelastic (NV) model is established to describe the interaction between the needle and the vein. An adaptive integral terminal sliding mode controller incorporating the NV model (NAITSMC) is developed to accurately track the desired preload force. Ultimately, the overall robotic micropuncture approach is applied to the retinal vein to enhance the success rate. The contributions of this article are summarized as follows.

- 1) A preload strategy is proposed to enhance the success rate of micropuncture by improving local stiffness, thereby ensuring a stable micropuncture process.
- 2) The NV model is developed to characterize the force response during the preload procedure. By adding a nonlinear spring element to the linear constitutive model, the nonlinearity and relaxation of the retinal vein can be simulated simultaneously.
- 3) The proposed preload force controller aims to achieve precise force tracking. The developed adaptive law developed is capable of estimating state-dependent lumped disturbances resulting from tissue uncertainty and respiratory motion, without requiring prior knowledge. An input constraint mechanism for speed is employed through an auxiliary system to ensure safe interaction.
- 4) Based on the open-sky porcine eye experiment, which utilized inflatable retinal veins and simulated respiratory motion, the effectiveness of the force modeling and the preload force controller has been validated. A preload force of 40  $\mu$ N is recommended to improve the success rate, while ensuring safety.

The rest of this article is organized as follows. In Section II, the robotic micropuncture approach with preload strategy is described. The NV model is first given on the basis of preload force control in Section III. Section IV presents the design of the NAITSMC for preload strategy. Section V verifies and discuss the effectiveness of the NV modeling, force control, and preload strategy performance based on comparative experiments. Finally, Section VI concludes this article.

# II. ROBOTIC MICROPUNCTURE

Consider a high-precision micromanipulator equipped with a needle. The force applied at the needle is measurable via a precise force sensor. Initially, the operator manually manipulates the needle to establish contact with the retinal vein, guided by the force feedback and the microscope view. As illustrated in Fig. 2(a) and (b), with predetermined motion and speed, the needle tip is robotically inserted in the axial direction. Based on

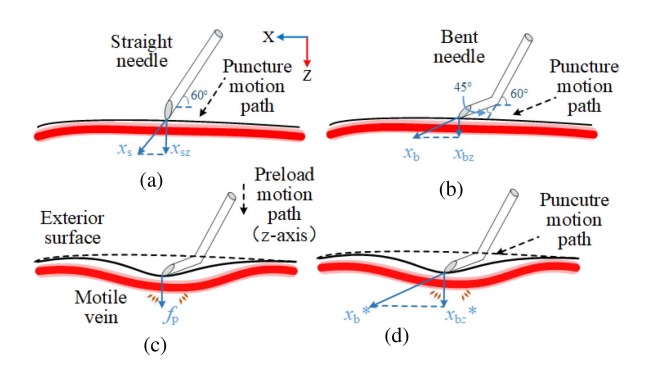


Fig. 2. Diagram of the micropuncture with preload strategy. (a) Micropuncture process via straight needle. (b) Micropuncture process via bent needle without preload. (c) Preload strategy before the micropuncture process. (d) Micropuncture process after the preload strategy.

the force signal, the operator can assess the micropuncture state (success or failure) for subsequent injection.

The objective of this article is to improve the success rate of micropuncture. However, the unstable needle-vein interaction poses challenges in ensuring a successful puncture with limited motion. In response to this issue, a robotic micropuncture scheme incorporating a preloading strategy is proposed to improve the success rate of micropuncture.

# A. Preload Strategy

There are two types of needles utilized in RVC surgery: The straight needle and the bent needle (the tip is  $45^{\circ}$  relative to the tool shaft). Due to the restriction of the needle to the scleral incision, the angle formed by the straight needle relative to the retina is larger ( $60^{\circ}$ ) [7]. The angle for the bent needle is smaller ( $15^{\circ}$ ). As illustrated in Fig. 2(a), from the safety perspective, the straight needle poses a larger motion in the *z*-axis, increasing the risk of double-puncture. The bent needle has more advantages in reducing the risk of double-puncture with clinical application [11]. However, as illustrated in Fig. 2(b), the bent needle results in less deformation in the *z*-axis at the contact point, which may lead to unstable contact during micropuncture. Thus, while the bent needle is generally regarded as safer than the straight needle, it presents challenges concerning successful micropuncture.

In light of this, this article draws upon clinical experience by initially preloading the retinal vein with a bent needle prior to executing the puncture procedure. As illustrated in Fig. 3, the nonlinear properties of the retina are demonstrated through the force-motion curve derived from the experiments. This result indicates that the larger deformation of retina result in higher stiffness. The deformation distribution resulting from the simulated needle-retina interaction is shown in Fig. 4. The larger preload force results in higher deformation and larger deformation area. Due to the nonlinear properties of retinal tissue, the increase in local deformation results in higher stiffness. Benefiting from the preload strategy, the higher stiffness can be maintained at the beginning of micropuncture. Thus, this approach can improve the success rate of micropuncture, while simultaneously reducing the risk of double-puncture.

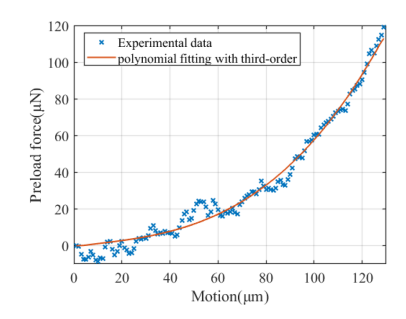


Fig. 3. Nonlinear property of the actual retinal tissue. The experimental force data are collected from needle preload on retinal vein of in vitro open-sky porcine eye at a speed of 0.1 mm/s in the *Z*-axis. The larger deformation results in higher stiffness (larger slope).

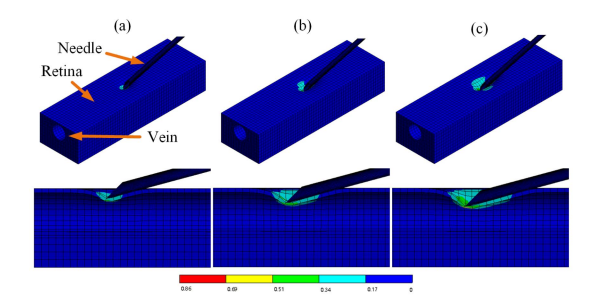


Fig. 4. Deformation diffusion of the stimulated retinal vein in ANSYS with different preload force. (a) 20  $\mu$ N. (b) 40  $\mu$ N. (c) 60  $\mu$ N. The color of the each element represents the strain. The first line shows the full view of the deformation area. The second line shows the section view of deformation. The Young's models and the Poisson's ratio of the retina is set as 0.03 MPa and 0.49 based on [27]. The micropuncture angle is 15°. The diameter of the needle and vein are 60  $\mu$ m and 200  $\mu$ m. The thickness of vein wall is 20  $\mu$ m.

#### B. Overall Workflow

Based on the proposed preload strategy outlined above, the robotic micropuncture workflow is segmented into two main steps: 1) *Preload:* As shown in Fig. 2(c), the needle robotically achieves precise automatic control of the preload force along the *z*-axis; 2) *Micropuncture:* As shown in Fig. 2(d), the axial micropuncture of the retinal vein is conducted via the needle with predetermined speed and displacement.

# III. NONLINEAR VISCOELASTIC MECHANICAL MODELING

As the soft tissue, the retina has viscoelastic characteristics. The most commonly used solid elements in viscoelastic models are spring and damping. The structure composed of these two solid elements can describe both relaxation and creep. Although spring-damper-based viscoelastic models have been shown to evaluate the mechanical response of soft tissues, the above methods are unable to describe the nonlinearity of the retinal vein. Based on the SLS model, the part of the linear spring is replaced with a nonlinear spring to further model the nonlinearity.

As shown in Fig. 5, the structure on the left side is a Maxwell model, which is composed of springs and dampers connected in series, and can describe the relaxation better. The relationship between force  $f_1$  and deformation  $x_1$  of the Maxwell model can

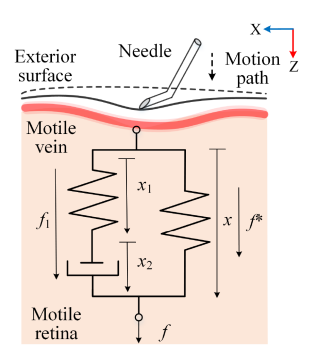


Fig. 5. NV model for motile retinal vein during preload path.

be expressed as [15]

$$\dot{x}_1 = \frac{1}{\eta} f_1 + \frac{1}{k_1} \dot{f}_1 \tag{1}$$

where  $k_1$  and  $\eta$  are the spring constant and the dashpot constant, respectively.  $\dot{f}_1$  is the first derivative of the force in the Maxwell model. The force of the entire NV model f can have [15]

$$f = f^* + f_1 \tag{2}$$

where the  $f^*=k^*(x)$  denotes the force of nonlinear spring. x denotes the deformation of nonlinear spring, as well as the total deformation of the NV model. Therefore, the entire NV model f can be further described as

$$f = k^*(x) + \eta \dot{x} - \frac{\eta}{k_1} \dot{f}_1.$$
 (3)

Based on (2) and (3), which further gives

$$f + \frac{\eta}{k_1}\dot{f} = k^*(x) + \left(\eta + \frac{\eta}{k_1}\frac{\mathrm{d}k^*(x)}{\mathrm{d}x}\right)\dot{x}.\tag{4}$$

In this article, a third-order polynomial is utilized to model the nonlinear spring. Finally, the NV model is expressed as

$$f + \frac{\eta}{k_1} \dot{f} = \sum_{i=1}^{3} a_i x^i + \left( \eta + \frac{\eta}{k_1} \sum_{i=1}^{3} i a_i x^{i-1} \right) \dot{x}$$
 (5)

where  $a_1, a_2$ , and  $a_3$  are the constants of the nonlinear spring. Moreover, as the linear spring  $F^* = k_0 x$  is considered, the NV model degrades to the SLS model [15]

$$f + \frac{\eta}{k_1}\dot{f} = k_0 x + \frac{\eta(k_0 + k_1)}{k_1}\dot{x}.$$
 (6)

Remark 1: For the application of standardized glass needles to achieve preload strategy, considering that Young's modulus of the glass needle (50 GPa [28]) is significantly different from that of the retinal tissue (0.03 MPa [27]), rigidity is assumed in the NV model. As for the use of flexible needle, needle deformation may affect the modeling performance. Furthermore, respiratory motion may lead to imprecision in modeling. To achieve precise preloading strategy, the subsequent design of force controller can compensate for the above-mentioned uncertainties and disturbances.

#### IV. FORCE CONTROL FOR PRELOAD STRATEGY

The implementation of the preload strategy depends on precise force control. However, there are parameter uncertainties and external disturbance in the mechanics of the retinal vein. The NAITSMC is proposed to achieve accurate preload force control.

# A. Dynamic Modeling

The NV model is transformed into the following dynamics:

$$\dot{f} = (Af + \sum_{i=1}^{3} B_i x^i) + \left(C + \sum_{i=1}^{3} D_i x^{i-1}\right) \dot{x}$$
 (7)

where  $A=-k_1/\eta$ ,  $B_i=-k_1a_i/\eta$ ,  $C=k_1$ , and  $D_i=ia_i$ . Considering retinal tissue parameter uncertainty as  $A=\hat{A}+\Delta A$ ,  $B_i=\hat{B}_i+\Delta B_i$ ,  $C=\hat{C}_i+\Delta C$ , and  $D_i=\hat{D}_i+\Delta D_i$ , with external respiratory movement disturbance d, the system dynamics can be obtained as

$$\dot{f} = (\hat{A}f + \sum_{i=1}^{3} \hat{B}_{i}x^{i}) + (\hat{C} + \sum_{i=1}^{3} \hat{D}_{i}x^{i-1})\dot{x} + d_{l}$$
 (8)

where  $d_l = (\Delta A f + \sum_{i=1}^3 \Delta B_i x^i) + (\Delta C + \sum_{i=1}^3 \Delta D_i x^{i-1}) \dot{x} + d \text{ denoted as the lumped disturbance.}$   $\hat{B}_i$ ,  $\hat{C}$ , and  $\hat{D}_i$  denoted as the nominal or identified value.  $\Delta A$ ,  $\Delta B_i$ ,  $\Delta C$ , and  $\Delta D_i$  denoted as the uncertainty of the parameters.

Let control input  $u=\dot{x}$ , the system dynamics can be modeled as

$$\dot{f} = \xi + gu + d_l \tag{9}$$

where  $\xi = \hat{A}f + \sum_{i=1}^3 \hat{B}_i x^i$ , and  $g = \hat{C} + \sum_{i=1}^3 \hat{D}_i x^{i-1}$ .

#### B. Disturbance Analysis

For  $d_l$ , it can be bounded as

$$|d_{l}| \leq |\Delta A||f| + \sum_{i=1}^{3} |\Delta B_{i}||x|^{i} + (|\Delta C| + \sum_{i=1}^{3} |\Delta D_{i}||x|^{i-1})|u| + |d|$$
(10)

where  $|\cdot|$  represents the norm. Assume that external disturbance and parameter uncertainty bounded by  $|d| < d_m, |\Delta A| < \Delta A_m, |\Delta B_i| < \Delta B_{im}, |\Delta C| < \Delta C_m, \text{ and } |\Delta D_i| < \Delta D_{im}.$  Consider the fragility of the retinal vein, the input u is constrained by  $|u| < u_m$ . The state-dependent  $d_l$  can be further bounded as

$$|d_l| \le \rho_0 + \rho_1 |x| + \rho_2 |x|^2 + \rho_3 |x|^3 + \rho_4 |f| \tag{11}$$

where  $\rho_0 = d_m + (\Delta C_m + \Delta D_m)u_m$ ,  $\rho_1 = \rho_2 = \Delta B_m + \Delta D_m u_m$ ,  $\rho_3 = \Delta B_m$ , and  $\rho_4 = \Delta A_m$ .

#### C. Controller Design

The control objective is that the preload force f can accurately track the desired force  $f_d$  with lumped disturbance. An integral sliding mode surface s is defined as [29]

$$s = e + c \int_0^t |e|^{\frac{1}{2}} \operatorname{sign}(e) d\tau \tag{12}$$

where  $e=f-f_d$  is denoted as the force tracking error. c is the positive constants.  $\mathrm{sign}(\cdot)$  is the symbolic function. The derivative of the sliding mode surface is as follows:

$$\dot{s} = \dot{e} + c|e|^{\frac{1}{2}}\operatorname{sign}(e). \tag{13}$$

Although large control input speeds up convergence, excessive preload speed may affect the stability of the closed-loop system. In particular, it is unsafe for application in fragile retinal vein without input constraint. For eliminating saturation value  $\Delta u$ , an adaptive law is designed using the state of the auxiliary system  $\theta$  as follows [30]:

$$\dot{\theta} = -K_3\theta - \frac{|gs\Delta u| + 0.5\Delta u^2}{\theta}F(\theta) + \Delta u \tag{14}$$

where  $\Delta u = u - u_o$ , the overall control law  $u = \text{sign}(u_o) \min\{|u_o|, u_m\}$ .  $u_o$  is the nominal control law.  $F(\theta)$  is the smooth nonlinear switching function, which can be represented as [31]

$$F(\theta) = \begin{cases} 0, |\theta| \le X_a \\ 1 - \cos\left(\frac{\pi}{2}\sin\left(\frac{\pi}{2}\frac{\theta^2 - X_a^2}{X_b^2 - X_a^2}\right)\right), \text{ otherwise} \\ 1, |\theta| \ge X_b \end{cases}$$
 (15)

where  $0 < X_a < X_b$  is utilized to avoid the singularity of the auxiliary system as  $\theta$  approaches zero. The auxiliary variable  $\theta$  is used to compensate for the influence of  $\Delta u$ , enabling the actual overall control law u to remain within  $u_m$ , while ensuring the gradual convergence of  $\theta$ .

Let  $\dot{s}=0$  without disturbance, the equivalent control law is obtained as  $u_{\rm eq}=-g^{-1}[\xi+c|e|^{\frac{1}{2}}{\rm sign}(e)-\dot{f}_d]$ . The switching law deal with disturbance can be obtained by reaching law as  $u_{\rm sw}=-g^{-1}[K_1s+K_2{\rm sign}(s)]$ . Combined with the auxiliary system (14), the overall nominal control law is obtained as

$$u_o = -g^{-1} [\xi + c|e|^{\frac{1}{2}} sign(e) - \dot{f}_d + K_1 s + K_2 sign(s) + \lambda \theta]$$
(16)

where

$$K_{2} = \sum_{i=0}^{3} \hat{\rho}_{i} |x|^{i} + \hat{\rho}_{4} |f|$$

$$\dot{\hat{\rho}}_{i} = -\alpha \hat{\rho}_{i} + |s| |x|^{i}, i = 0, 1, 2, 3$$

$$\dot{\hat{\rho}}_{4} = -\alpha \hat{\rho}_{4} + |s| |f|$$
(17)

where  $0 < \alpha < 1$ .  $K_1$  and  $\lambda$  are the positive constants. Based on the disturbance analysis (11) based on dynamics (9), the designed gain  $K_2$  in NAITSMC can adaptively compensate the state-dependent lumped disturbance  $d_l$  without the prior upper bound. The diagram of the NAITSMC system is shown as Fig. 6.

# D. Stability Analysis

The following lemmas are used for the stability analysis. Lemma 1 ([32]): Assume that  $(a,b) \in \Re$  and holds  $\frac{1}{p} + \frac{1}{q} = 1$ , with p > 1, q is nonzero number. The following Young's inequality can be obtained:  $ab \leq \frac{a^p}{p} + \frac{b^q}{q}$ .

Lemma 2 ([33]): Considering nonlinear system  $\dot{x} = f(x, u)$ , assume the initial value is bounded, if a continuous and positive definite Lyapunov function V(x) with the form as:  $\varrho_1(|x|) \le$ 

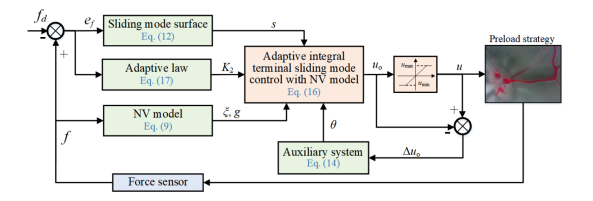


Fig. 6. Diagram of NAITSMC.

 $V(x) \leq \varrho_2(|x|)$  and  $V(x) \leq -\varrho V(x) + \vartheta$ , where  $\varrho$  and  $\vartheta$  are positive numbers. The system trajectory x(t) is uniformly ultimately bounded (UUB).

Considering the force dynamics (9) of the retinal vein under the lumped disturbance  $d_l$  and the input saturation  $u_m$ , the NAITSMC (16) with the auxiliary system (14) can guarantee that the closed-loop system is stable. The sliding surface s, auxiliary state variable  $\theta$ , and estimation error  $\tilde{\rho}_i$  are UUB. Select the Lyapunov function candidate as

$$V = \frac{1}{2}s^2 + \frac{1}{2}\theta^2 + \frac{1}{2}\sum_{i=0}^4 \widetilde{\rho}_i^2$$
 (18)

where  $\tilde{\rho}_i = \hat{\rho}_i - \rho_i$ . Taking the first-order derivative of V yields

$$\dot{V} = s\dot{s} + \theta\dot{\theta} - \sum_{i=0}^{4} \widetilde{\rho}_{i} \hat{\overline{\rho}}_{i}. \tag{19}$$

Based on the sliding mode surface and NAITSMC law, we have

$$\dot{s} = \dot{e} + c|e|^{\frac{1}{2}} \operatorname{sign}(e)$$

$$= -K_1 s - \lambda \theta - K_2 \operatorname{sign}(s) + g\Delta u + d_l. \tag{20}$$

So that, the derivation of the V gives to

$$\dot{V} = -K_1 s^2 - \lambda \theta s - K_2 |s| + gs\Delta u + d_l s$$

$$-K_3 \theta^2 - (|gs\Delta u| + 0.5\Delta u^2) F(\theta)$$

$$+ \Delta u \theta - \sum_{i=0}^4 \widetilde{\rho}_i \hat{\rho}_i. \tag{21}$$

Notice that the inequalities  $-\lambda\theta s \leq \frac{1}{2}\lambda^2 s^2 + \frac{1}{2}\theta^2$ ,  $\Delta u\theta \leq \frac{1}{2}\Delta u^2 + \frac{1}{2}\theta^2$ , and  $\sum_{i=0}^4 \widetilde{\rho}_i \widehat{\rho}_i \leq \sum_{i=0}^4 (\frac{1-2\varepsilon}{2\varepsilon}\widetilde{\rho}_i^2 + \frac{\varepsilon}{2}\rho_i^2)$  can be satisfied according to Lemma 1, the derivation of the V further leads to

$$\begin{split} \dot{V} &\leq -(K_{1}-0.5\lambda^{2})s^{2} - (K_{3}-1)\theta^{2} + |d_{l}|\,|s| \\ &- K_{2}\,|s| - \sum_{i=0}^{4} \widetilde{\rho}_{i}\dot{\widehat{\rho}}_{i} + 0.5\Delta u^{2}(1-F(\theta)) \\ &- |gs\Delta u|\,(F(\theta) - \mathrm{sign}(gs\Delta u)) \\ &\leq -(K_{1}-0.5\lambda^{2})s^{2} - (K_{3}-1)\theta^{2} \\ &- |gs\Delta u|\,(F(\theta) - \mathrm{sign}(gs\Delta u)) + \sum_{i=0}^{4} \alpha\widetilde{\rho}_{i}\widehat{\rho}_{i} \\ &+ 0.5\Delta u^{2}(1-F(\theta)) \\ &\leq -(K_{1}-0.5\lambda^{2})s^{2} - (K_{3}-1)\theta^{2} \\ &- |gs\Delta u|\,(F(\theta) - \mathrm{sign}(gs\Delta u)) \\ &+ 0.5\Delta u^{2}(1-F(\theta)) \end{split}$$

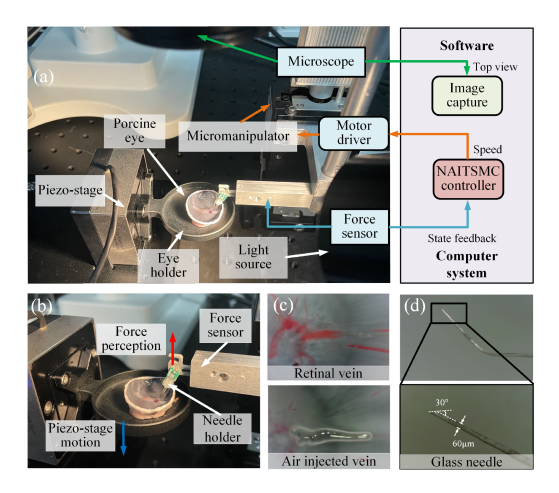


Fig. 7. Experimental platform of the robotic micropuncture. (a) Hardware and software for the micropuncture. (b) Enlarged view of the force sensor and porcine eye. The glass needle is fixed to the probe of the force sensor via holder (green). (c) Original retinal vein and the air injected vein. (d) Enlarged view of the glass needle tip.

$$+\alpha \sum_{i=0}^{4} \left( \frac{1-2\varepsilon}{2\varepsilon} \widetilde{\rho}_i^2 + \frac{\varepsilon}{2} \rho_i^2 \right). \tag{22}$$

Now, the following two cases are proved separately.

Case 1: For  $F(\theta) < 1$ , with the inequality  $gs\Delta u \leq \frac{1}{2}s^2 + \frac{1}{2}g^{2^*}s^2$  satisfied according to Lemma 1, the derivation of the V can be obtained as  $\dot{V} \leq -\Psi_1 + \Omega_1$ , where  $\Psi_1 = \min\{2K_1 - \lambda^2 - 1, 2K_3 - 2, \frac{\alpha(2\varepsilon-1)}{\varepsilon}\}$  and  $\Omega_1 = \frac{\alpha\varepsilon}{2}\sum_{i=0}^4 \rho_i^2 + \frac{1+g^2}{2}\Delta u^2$ . Case 2: For  $F(\theta) = 1$ , the derivation of the V can be obtained as  $\dot{V} \leq -\Psi_2 + \Omega_2$ , where  $\Psi_2 = \min\{2K_1 - \lambda^2, 2K_3 - 2, \frac{\alpha(2\varepsilon-1)}{\varepsilon}\}$  and  $\Omega_2 = \frac{\alpha\varepsilon}{2}\sum_{i=0}^4 \rho_i^2$ . According to two cases, we can further obtain that  $\dot{V} \leq -\Psi + \Omega$ , where  $\Psi = \min\{\Psi_1, \Psi_2\}$  and  $\Omega = \max\{\Omega_1, \Omega_2\}$ , we can further get  $V(t) \leq V(0)e^{-\Phi t} + \frac{\Omega}{\Phi}$ . Therefore, the V is UUB by the Lyapunov stability theory according to Lemma 2.

Remark 2: Fast response and high precision can be achieved by appropriate parameter selection. The fixed parameters c and  $K_1$  mainly affect the performance. The big value of c and  $K_1$  will cause faster convergence speed and lower error, but will obtain an unstable transient response. A reasonable guideline is to first adjust the  $K_1$  to achieve a faster convergence with lower oscillation. Then, further adjust c so that the steady-state error is reduced without significant transient peaks. According to stability analysis,  $K_1$ ,  $\lambda$ , and  $K_3$  need to satisfy  $2K_1 - \lambda^2 - 1 > 0$ , and  $K_3 > 1$ . A large value  $\alpha$  will produce chattering, while a small value  $\alpha$  will increase the convergence time and reduce robustness. The  $K_a$  and  $K_b$  are the parameters of the auxiliary system that  $0 < K_a < K_b$  need to be satisfied.

# V. EXPERIMENTS

# A. Experimental Setup

The experimental system is illustrated in Fig. 7. A fixed holder connected to the piezo-stage (Scanner65-x. SP-NK, MultiFields Tech) is employed to support the porcine eye. The piezo-stage is used to simulate the respiratory motion. A light source (BG-II,

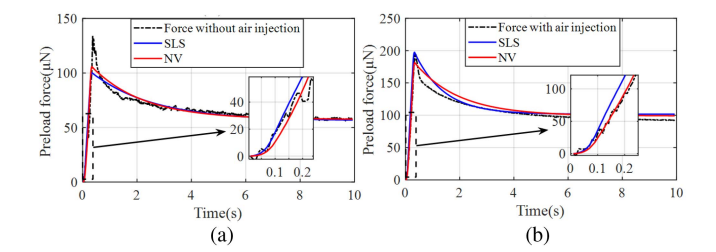


Fig. 8. Preload force modeling results of the retinal vein with 0.5 mm/s. (a) Preload force of vein without air injection. (b) Preload force of vein with air injection.

WSoptics) is utilized to illuminate the retina for observation. A surgical microscope (MSD204, Murzider), equipped with a CCD camera, is positioned above the porcine eye to capture images of the retina. The motorized X-Y-Z micromanipulator (MX7600, Siskiyou) is responsible for the precise motion of the needle. The movement of the micromanipulator is controlled by an upper computer and motor driver. The control algorithm is implemented in C++ environment in the host computer. As shown in Fig. 7(b), the glass needle is fixed on the force sensor (Nators, NSF-B, and resolution:  $0.5~\mu N$ ) to collect force data for offline modeling and online control. The sampling frequency of the force sensor is 100 Hz. The force signal is filtered using a moving average filter with a window size of five elements.

As illustrated in Fig. 7(c), fresh retinal vein and the air injected vein (to simulate the blood pressure [34]) are utilized for the experiments. The veins within about 200  $\mu$ m are distributed in the retina. The reduction of intraocular pressure in an open-sky scenario can lead to localized retinal detachment. To ensure consistent results, the veins adjacent to the optic disc are employed to validate the proposed procedure. In Fig. 7(d), the diameter of the glass needle is approximately 60  $\mu$ m. It is oriented 60° from the X–Y plane, and the end bend angle is 45°, resulting in a micropuncture angle of 15°. The bevel angle is 30° to ensure effective micropuncture.

#### B. Preload Force Modeling Performance

To apply the NV model for force control in the preload strategy, the parameters  $a_1$ ,  $a_2$ ,  $a_3$ ,  $\eta$ , and  $k_1$  need to be identified. This identification process is based on the force data collected during the preload operation. In particular, the needle tip is moved to make contact with the retinal vein, ensuring that the direction of the needle aligns with the center of the vein. At this point, downward movement is initiated at a speed ranging from 0.1 to 0.5 mm/s, during which force data is collected. The total motion at varying speeds is 0.15 mm. To verify the applicability of the NV model in the real eyes, the original veins and air injected veins are used for modeling. The root mean square error (RMSE) serves as the objective function for parameter identification. The RMSE and the R-Square  $(R^2)$  are utilized to assess the modeling accuracy of the force during preload and puncture procedures. A lower RMSE or a higher R<sup>2</sup> indicates superior accuracy.

Fig. 8(a) illustrates the force response curve of two veins generated by the preload strategy at a speed of 0.5 mm/s. As the

TABLE I
PARAMETER IDENTIFICATION RESULTS FOR PRELOAD FORCE MODELING

Vein type	Model	Parameters	RMSE	$\mathbb{R}^2$
without air injected	SLS	$k_0$ =0.38 N/m, $\eta$ =0.72 Ns/m, $k_1$ =0.32 N/m	6.16	0.86
	NV	$a_1$ =2.53e-7 N/m, $a_2$ =2556.65 N/m², $a_3$ =2081.42 N/m³, $\eta$ =0.64 Ns/m, $k_1$ =0.34 N/m	4.64	0.92
with air injected	SLS	$k_0$ =0.68 N/m, $\eta$ =0.79 Ns/m, $k_1$ =0.74 N/m	8.89	0.85
	NV	$a_1$ =0.28 N/m, $a_2$ =2571.16 N/m <sup>2</sup> , $a_3$ =2309.35 N/m <sup>3</sup> , $\eta$ =0.96 Ns/m, $k_1$ =0.59 N/m	6.82	0.90

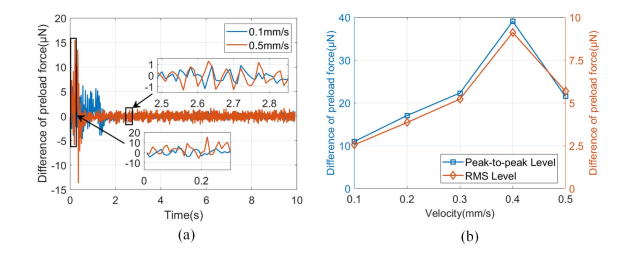


Fig. 9. Mechanical vibration of the interaction force. (a) Force signal comparation between 0.1 mm/s and 0.5 mm/s. (b) Peak-to-peak and root mean square level of force signal under variant speeds.

needle initiates movement, the contact force gradually increases. The needle stopped at approximately 0.3 s, after which the force diminishes gradually and converges, demonstrating a typical relaxation phenomenon. Due to the air injection, the peak force at the same preload motion will be larger. The 'fmincon' function from the MATLAB optimization toolbox is employed to solve the optimal parameters. Based on the force data, the parameters of the SLS and NV models with different vein are identified and presented in Table I. The force modeling curve at 0.5 mm/s as shown in Fig. 8(b), exhibits nonlinearity during the motion of the needle. The calculated RMSE and R<sup>2</sup> at various speeds are depicted in Fig. 8(c) and (d). It can be known from Table I that under different veins, the NV model is superior to the SLS model in both RMSE and R<sup>2</sup>. The NV model demonstrates superior capability in simulating the nonlinearity and viscoelastic characteristics of the retinal vein.

# C. Preload Force Control Performance

The preload force control is carried out based on the identified NV model. Two cases are used to verify the performance of NAITSMC. One is to verify on the original vein and air injected vein without simulated respiratory motion, and the other is to verify on the air injected vein under different respiratory motion amplitudes. According to the parameter selection guideline from Remark 2 with trial-and-error strategy, the parameters of the NAITSMC are selected as:  $K_1 = 8$ , c = 1.5,  $K_3 = 1.1$ ,  $\lambda = 0.001$ ,  $\alpha = 0.1$ ,  $X_a = 0.01$ , and  $X_b = 0.1$ . The hyperbolic tangent function is adopted instead of the sign function to reduce chattering. Considering the influence of mechanical vibration on force control, the force response vibration at different speeds is analyzed. As shown in Fig. 9(a), the force difference produces

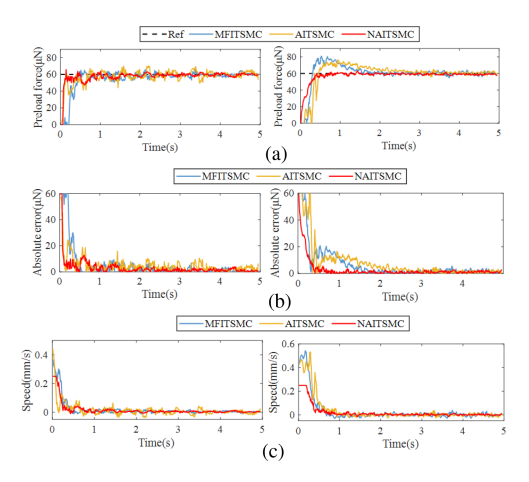


Fig. 10. Experimental results of the preload force control of 60  $\mu$ N. The left and right figures show the force control results of the original vein and the air injected vein, respectively. (a) Force tracking. (b) Force error. (c) Control input.

obvious vibration during the motion phase, but decreases significantly in the relaxation phase. The force difference at 0.5 mm/s is significantly higher than that at 0.1 mm/s. The vibration is characterized by the peak-to-peak level and the root mean square of the force difference during the moving phase. It can be seen that both indicators are larger at the speed of 0.3–0.5 mm/s in Fig. 9(b). The large speed produce vibration that degrades control performance and safety. So the  $u_m=0.25$  is considered as the upper constraint for control input.

To verify the performance of the NAITSMC, the MFITSMC [23], and AITSMC [24] are used for comparison. The control law of two methods are expressed as

$$u_{\text{MFITSMC}} = u_{t-t_s} - g^{-1} [\dot{f}_{t-t_s} + k_1 s + k_2 \text{sign}(s) - \dot{f}_d + \sigma_1 e + \sigma_1 \sigma_2 |e_f|^{\rho} \text{sign}(e_f)]$$
 (23)

where subscript of  $t-t_s$  denotes its value at the delayed time of  $t_s$ 

$$\begin{split} u_{\text{AITSMC}} &= -g^{-1} [\hat{\Xi}^{A} f + \sum_{i=1}^{3} \hat{\Xi}_{i}^{B} x^{i} - \dot{f}_{d} + \sigma_{1} e \\ &+ \sigma_{1} \sigma_{2} |e_{f}|^{\rho} \text{sign}(e_{f}) + \hat{\kappa} \text{sat}(s/\phi)] \end{split} \tag{24}$$

where  $\dot{\bar{\Xi}}^A=Psf$ ,  $\dot{\bar{\Xi}}^B_i=Psx^i$ , and i=1,2,3.  $\dot{\hat{\kappa}}=|s|$ .  $\mathrm{sat}(s/\phi)=\mathrm{sign}(s)$ , if  $|s|>\phi$  or  $\mathrm{sat}(s/\phi)=s/\phi$ , if  $|s|\leq\phi$ . P and  $\phi$  are the positive constants. The parameters of MFITSMC are selected as:  $k_1=8$ ,  $k_2=1$ ,  $\sigma_1=\sigma_2=2.5$ , and  $\rho=0.5$ . The parameters of AITSMC are selected as:  $\sigma_1=\sigma_2=2.5$ ,  $\rho=0.5$ ,  $\phi=0.05$ , and  $\rho=0.5$ .

A 20, 40, and 60  $\mu$ N are set as the desired forces, respectively. During the preload force control experiment, the needle is aligned above the retinal vein in the field of view of the microscope, and then the force controller is activated to achieve the preload operation. For the experiment considering respiratory, the piezo-stage generates a sinusoidal motion with period of 5 s, corresponding to the average human respiratory cycle [35]. The mean absolute error (MAE) and RMSE are selected to assess the control performance. The lower values of these two statistical errors indicate higher control precision. The performance of different retinal veins is first verified. Fig. 10 shows the preload

TABLE II
PRELOAD FORCE CONTROL PERFORMANCE WITH DIFFERENT TYPES OF
VEIN

Vein type	Desired force	Error	MFITSMC	AITSMC	NAITSMC
without air injected	20	MAE	4.34	2.52	2.49
	20	RMSE	6.68	4.5	4.33
	40	MAE	4.51	4.71	3.1
	40	RMSE	8.58	9.12	7.28
	60	MAE	5.53	4.96	2.98
		RMSE	14.43	8.71	7.44
with air injected	20	MAE	1.59	1.57	1.25
	20	RMSE	3.02	2.73	2.25
	40	MAE	5.15	4.87	3.48
	40	RMSE	10.45	8.72	7.67
	60	MAE	6.37	7.61	2.70
	00	RMSE	13.74	14.59	7.29

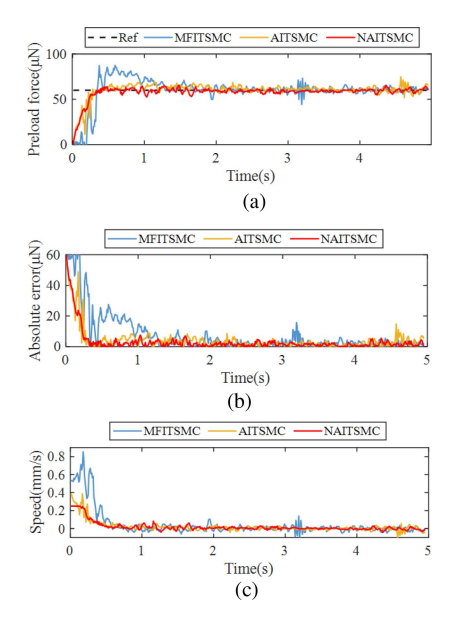


Fig. 11. Performance comparison of the preload force control. The desired force is 60, and the amplitude of simulated respiratory motion is  $20\mu m$ . (a) Force tracking. (b) Force error. (c) Control input.

force tracking results with three controllers. As shown in Fig. 10(a), with two types of retinal vein, the NAITSMC can both track the desired force with fast response. At the same time, NAITSMC has less error in Fig. 10(b). Fig. 10(c) further shows that the NAITSMC has a lower maximum speed (constrained in 0.25 mm/s) than the other two controller. Table II further shows the specific results of three controllers in terms of MAE and RMSE. It can be seen that due to the stronger uncertainty of the air injected vein, the performance of other controllers declines, but the proposed controller still maintains better precision.

The robustness of the proposed controller is further verified by simulating the disturbance of respiratory motion. The simulated respiratory motion of the piezo-stage adopts sinusoidal displacement. The amplitudes are chosen as 20, 40, and 60  $\mu$ m. As shown in Fig. 11(a), NAITSMC enables the preload force to converge rapidly to 60  $\mu$ N, while the transition process

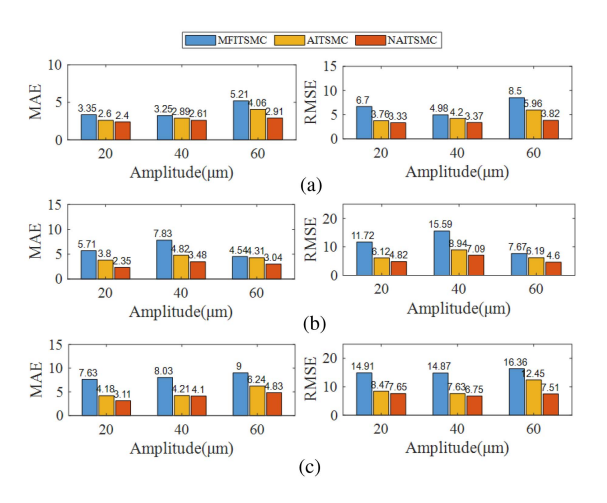


Fig. 12. Comparison of statistical errors under variant respiratory motion amplitudes. (a) Desired force of 20  $\mu$ N. (b) Desired force of 40  $\mu$ N. (c) Desired force of 60  $\mu$ N.

is more stable. Fig. 11(b) shows that NAITSMC still has a lower steady-state error under the disturbance of respiratory motion. Fig. 11(c) shows that a constraint speed reduces the oscillation phenomenon, and has lower chattering in the steadystate. Fig. 12 presents the performance comparison of the three controllers under different amplitudes of respiratory motion. With the increase of respiratory motion amplitude, NAITSMC is able to reduce MAE and RMSE to within 4.83 and 7.65  $\mu$ N, respectively. The maximum MAE and RMSE of MFITSMC are 9 and 16.36  $\mu$ N, respectively, while those of AITSMC are 6.24 and 12.45  $\mu$ N, respectively. Compared with MFITSMC and AITSMC, the maximum MAE of NATISMC decreased by 46.33% and 22.6%, respectively, and the RMSE decreased by 53.24% and 38.55%, respectively. Based on the statistical error in Table II and Fig. 12, NAITSMC can effectively cope with the uncertainty of vein and respiratory disturbance, maintain better preload force precision and robustness.

# D. Robotic Micropuncture Performance With Preload Strategy

Based on the designed NAITSMC, selecting an appropriate preload force is anticipated to enhance the micropuncture success rate with limited motion. Specifically, the desired preload forces of 0, 20, 40, and 60  $\mu$ N are selected for preload, with axial puncture performed following this selection. The micropuncture motion is set at 0.8 mm, and micropuncture speeds are established at 0.5 mm/s and 1 mm/s, respectively. The micropuncture experiments are conducted ten times for each preload force and speed combination. Fig. 13 illustrates the process of a successful micropuncture in a microscopic view. Upon successful micropuncture of the retinal vein, the vein wall demonstrates a notable rebound. Corresponding to the image, the typical force curve is presented in Fig. 14. The success of robotic micropuncture can be judged by the change characteristics of force signal [36], [37]. The force associated with failed micropuncture exhibits a characteristic relaxation phenomenon. From the two successful micropuncture, the corresponding force curves reveal a rapid

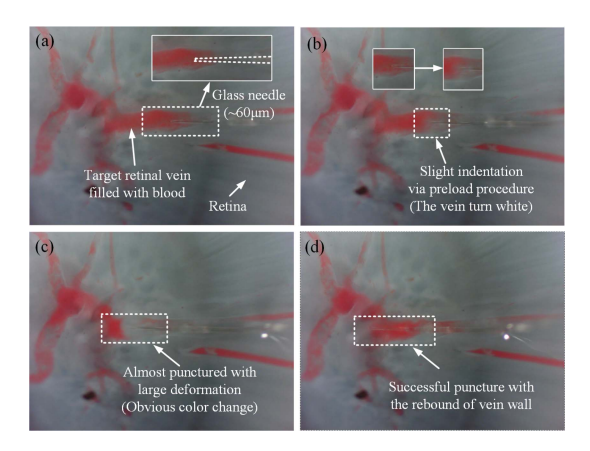


Fig. 13. Microscope view of a successful puncture process. (a) Needle contact with the vein. (b) Needle begin the motion. (c) Vein is about to be pierced with maximum deformation. (d) Vein is pierced with tissue rebound.

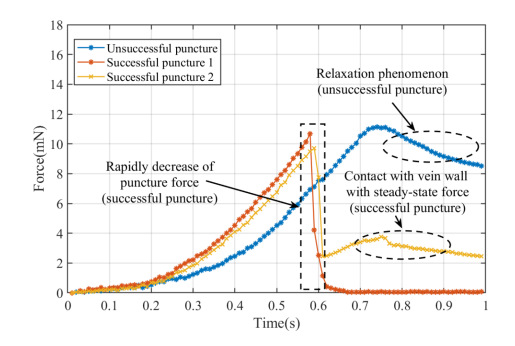


Fig. 14. Examples of the successful and failed puncture cases.

reduction near 0.6 s. The distinction between these two force curves lies in the behavior following the successful puncture: The first curve rapidly declines to near zero at 0.58 s, whereas the second curve exhibits an initial decline followed by an increase, culminating in a relaxation phenomenon. This observation can be attributed to the fact that, in the first scenario, the needle tip made less contact with the second vein wall (0.046 mN). In contrast, in the second scenario, the needle contacted the second vein wall, continued to advance after the successful puncture, thereby generating an obvious steady-state force (2.712 mN). For the sake of safe surgical practice, it is preferable to achieve the first curve and avoid the second curve, even in the absence of double-puncture.

Combining the cases on successful and failed robotic micropuncture, Fig. 15 illustrates the influence of preload force on success rate, steady-state force, peak force with failed puncture, peak force with successful puncture, puncture time, and deformation. As shown in Fig. 15(a), under two speeds, the success rate increased significantly with the increase of preload force. This observation indicates that the implementation of preload strategy effectively enhances the success rate. Conversely, Fig. 15(b) indicates that the steady-state force increases alongside the preload force. This phenomenon can be attributed to the compression of the retinal vein by the preload force, which increases the risk of the needle contacting the second vein wall

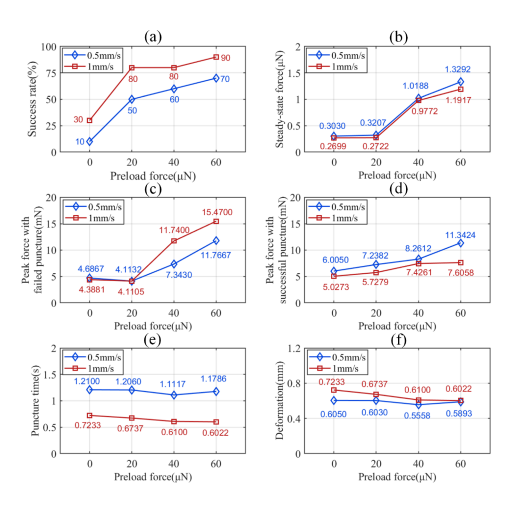


Fig. 15. Preload performance with different preload force. (a) Success rate. (b) Steady-state force of successful puncture. (c) Peak force of successful puncture. (d) Peak force of failed puncture. (e) Puncture time of successful puncture. (f) Deformation of successful puncture.

after a successful puncture. The comparison between Fig. 15(c) and (d) shows that the peak force of failed puncture is smaller than that of successful puncture when there is no preload force or low preload force ( $20~\mu N$ ), indicating unstable contact, which makes it difficult for veins to be punctured. With the increase of preload force, the peak force of failed puncture is higher than that of successful puncture. The preload strategy can improve the micropuncture performance as much as possible. As shown in Fig. 15(e), the punctured time is not significantly affected by the preload force, and speed is the main factor that significantly affects the puncture time. The deformation in Fig. 15(f) gently decreases as the preload force increases. The compression of the local tissue by the preload strategy reduces the deformation space of the vein wall, which also means that the micropuncture procedure is more stable.

#### E. Discussion

1) Extension of the Force Model: The experimental results show that the NV model can accurately model force response under different inner pressures. To improve the applicability of the NV model, it is recommended that practitioners can collect the force data of live retinal vein more extensively, to obtain the range of parameter uncertainties, thereby guiding the reliable optimization of controller parameters and enabling the controller to be better applied preload strategy in vivo experiments. The interaction between retinal veins and needles is not only affected by blood pressure, but may also be influenced by the material of the needle. The factor of needle deformation can be further considered in the NV model to ensure the applicability of the modeling.

2) Reason of the Success Rate Improvement: According to the simulation of the strain (see Fig. 4), with the increase of the preload force, the high-strain elements (from blue to yellowgreen) gradually diffuse. Due to the nonlinear characteristics of retinal tissue, the preload area has a high stiffness, which makes the overall micropuncture process more stable. Combined with

the experimental results on Fig. 15(c) and (d), the larger preload force (from 40 to 60  $\mu$ N) will produce larger micropuncture force, which is conducive to pierce the vein wall. Simulation and experimental analysis verified that the preload strategy is beneficial to improve the success rate of micropuncture.

- 3) Determined the Appropriate Preload Force: Selecting the appropriate preload force is crucial for ensuring a successful surgical outcome, while simultaneously mitigating the risk of tissue damage. The damage related to preload can be measured by two forces. One is the peak force with successful puncture, and the other is the contact force with the second vein wall (steady-state force). Although the puncture force is a necessary damage, it is expected to be reduced. Based on Fig. 15(a) and (b), an optimal preload force of  $40~\mu N$  is recommended, as this value yields a higher success rate (maximum 80%) with lower puncture peak force (maximum mean value of 8.2612 mN), while avoiding excessive steady-state force (maximum mean value of 1.0188 mN).
- 4) Selection of Surgical Needles: The lower-cost glass needle is adopted for the experiment in this article. However, the glass needle is prone to breakage in real surgeries, which may cause damage to the retinal tissue [8]. It is recommended that practitioners use glass needles in in vitro experiments and commercial metal needles in actual surgeries. Moreover, it is considered to produce glass needles with the same structural parameters as the metal needles (such as diameter, bevel shape, bevel tip orientation, etc.) for testing to ensure the reliability of the metal needles promoted for commercial use. Although the characteristics of metal needles and glass needles are slightly different, thanks to the adaptive ability of NAITSMC, the precision of applying preload strategy with metal needles can still be guaranteed.
- 5) Limitations Brought by Scleral Incision: In this article, experiments are conducted using open-sky porcine eyes. Real retinal surgery is limited by the constraints of scleral incision, resulting in additional collisions caused by respiratory motion and problems with sensor deployment. For the collision between the scleral incision and the surgical tools, it is recommended to suppress the accidental movement through remote center of motion mechanism and the compensation algorithm [5]. Combined with the robustness of NAITSMC, the disturbance caused by respiratory motion can be further reduced. Furthermore, the interaction force at the scleral incision (order of mN) can mask the preload force at the needle tip (order of  $\mu N$ ). This requires that the force sensor be deployed at the needle tip rather than the manipulator to ensure the reliable measurement of the preload force. Furthermore, to ensure the drug delivery function, deploying a very precise fiber bragg gratings sensor to the needle tip is a feasible solution [37].

#### VI. CONCLUSION

To enhance the success rate of micropuncture procedure in RVC, an automatic preload strategy is proposed. The overall methodology initially employs an NV model to describe the nonlinear and relaxation characteristics of the force response. A stable needle-vein contact is subsequently achieved through

preload force control utilizing NAITSMC. The validation using open-sky porcine eyes confirms that the preload strategy results in a success rate is up to 90%. This streamlined robotic micropuncture scheme for RVC is anticipated to be implemented in clinical practice.

#### REFERENCES

- [1] L. Nicholson, S. J. Talks, W. Amoaku, K. Talks, and S. Sivaprasad, "Retinal vein occlusion (RVO) guideline: Executive summary," *Eye*, vol. 36, no. 5, pp. 909–912, 2022.
- [2] M. Ho, D. T. Liu, D. S. Lam, and J. B. Jonas, "Retinal vein occlusions, from basics to the latest treatment," *Retina*, vol. 36, no. 3, pp. 432–448, 2016.
- [3] M. K. Tameesh et al., "Retinal vein cannulation with prolonged infusion of tissue plasminogen activator (T-PA) for the treatment of experimental retinal vein occlusion in dogs," *Amer. J. Ophthalmol.*, vol. 138, no. 5, pp. 829–839, 2004.
- [4] J. N. Weiss and L. A. Bynoe, "Injection of tissue plasminogen activator into a branch retinal vein in eyes with central retinal vein occlusion," *Ophthalmol.*, vol. 108, no. 12, pp. 2249–2257, 2001.
- [5] K. Willekens et al., "Phase I trial on robot assisted retinal vein cannulation with ocriplasmin infusion for central retinal vein occlusion," *Acta Ophthalmologica*, vol. 99, no. 1, pp. 90–96, 2021.
- [6] A. Gijbels et al., "In-human robot-assisted retinal vein cannulation, a world first," Ann. Biomed. Eng., vol. 46, pp. 1676–1685, 2018.
- [7] M. J. Gerber, J.-P. Hubschman, and T.-C. Tsao, "Automated retinal vein cannulation on silicone phantoms using optical-coherence-tomographyguided robotic manipulations," *IEEE/ASME Trans. Mechatron.*, vol. 26, no. 5, pp. 2758–2769, Oct. 2021.
- [8] K. Willekens et al., "Robot-assisted retinal vein cannulation in an in vivo porcine retinal vein occlusion model," *Acta Ophthalmologica*, vol. 95, no. 3, pp. 270–275, 2017.
- [9] K. A. van Overdam, T. Missotten, and L. H. Spielberg, "Updated cannulation technique for tissue plasminogen activator injection into peripapillary retinal vein for central retinal vein occlusion," *Acta Ophthalmologica*, vol. 93, no. 8, pp. 739–744, 2015.
- [10] M. Ourak et al., "Combined oct distance and fbg force sensing cannulation needle for retinal vein cannulation: In vivo animal validation," *Int. J. Comput. Assist. Radiol. Surg.*, vol. 14, pp. 301–309, 2019.
- [11] X. Gao et al., "A compact 2-DOF cross-scale piezoelectric robotic manipulator with adjustable force for biological delicate puncture," *IEEE Trans. Robot.*, vol. 40, pp. 4561–4577, 2024.
- [12] M. D. de Smet et al., "Robotic assisted cannulation of occluded retinal veins," *PLoS One*, vol. 11, no. 9, 2016, Art. no. e0162037.
- [13] Y. Kobayashi et al., "Enhanced targeting in breast tissue using a robotic tissue preloading-based needle insertion system," *IEEE Trans. Robot.*, vol. 28 no. 3 pp. 710–722. Jun. 2012.
- vol. 28, no. 3, pp. 710–722, Jun. 2012.

  [14] H. Zhang et al., "An FBG-based 3-DOF force sensor with simplified structure for retinal microsurgery," *IEEE Sensors J.*, vol. 22, no. 15, pp. 14911–14920, Aug. 2022.
- [15] H. Liu, D. P. Noonan, Y. H. Zweiri, K. A. Althoefer, and L. D. Seneviratne, "The development of nonlinear viscoelastic model for the application of soft tissue identification," in *Proc. IEEE/RSJ Int. Conf. Intell. Robots Syst.*, 2007, pp. 208–213.
- [16] Á. Takács, J. K. Tar, T. Haidegger, and I. J. Rudas, "Applicability of the Maxwell-Kelvin model in soft tissue parameter estimation," in *Proc. IEEE* 12th Int. Symp. Intell. Syst. Informat., 2014, pp. 115–119.
- [17] S. Kang, X. Yang, Y. Li, H. Wu, and T. Li, "A fractional viscoelastic mechanical model for speed optimization of robotic cell microinjection," *IEEE/ASME Trans. Mechatron.*, vol. 29, no. 6, pp. 4514–4525, Dec. 2024.
- [18] L. Han, H. Wang, Z. Liu, W. Chen, and X. Zhang, "Vision-based cutting control of deformable objects with surface tracking," *IEEE/ASME Trans. Mechatron.*, vol. 26, no. 4, pp. 2016–2026, Apr. 2021.
- [19] M. Ferrara, G. Lugano, M. T. Sandinha, V. R. Kearns, B. Geraghty, and D. H. Steel, "Biomechanical properties of retina and choroid: A comprehensive review of techniques and translational relevance," *Eye*, vol. 35, no. 7, pp. 1818–1832, 2021.
- [20] Z. Sun, Z. Wang, and S. J. Phee, "Force feedback without sensor: A preliminary study on haptic modeling," in *Proc. 4th IEEE RAS & EMBS Int. Conf. Biomed. Robot. Biomechatron.*, 2012, pp. 1182–1187.

- [21] R. de Kinkelder et al., "Heartbeat-induced axial motion artifacts in optical coherence tomography measurements of the retina," *Invest. Ophthalmol. Vis. Sci.*, vol. 52, no. 6, pp. 3908–3913, 2011.
- [22] P. Xiang et al., "Learning-based high-precision force estimation and compliant control for small-scale continuum robot," *IEEE Trans. Automat. Sci. Eng.*, vol. 21, no. 4, pp. 5389–5401, Oct. 2024.
- [23] J. Lee, M. Jin, N. Kashiri, D. G. Caldwell, and N. G. Tsagarakis, "Inversion-free force tracking control of piezoelectric actuators using fast finite-time integral terminal sliding-mode," *Mechatronics*, vol. 57, pp. 39–50, 2019.
- [24] Z. Feng, W. Liang, J. Ling, X. Xiao, K. K. Tan, and T. H. Lee, "Precision force tracking control of a surgical device interacting with a deformable membrane," *IEEE/ASME Trans. Mechatron.*, vol. 27, no. 6, pp. 5327–5338, Dec. 2022.
- [25] Y. Wei and Q. Xu, "A survey of force-assisted robotic cell microinjection technologies," *IEEE Trans. Automat. Sci. Eng.*, vol. 16, no. 2, pp. 931–945, Apr. 2019.
- [26] X. Liang et al., "Adaptive human–robot interaction torque estimation with high accuracy and strong tracking ability for a lower limb rehabilitation robot," *IEEE/ASME Trans. Mechatron.*, vol. 29, no. 6, pp. 4814–4825, Dec. 2024.
- [27] Y. Yan, H. Shi, Y. Zhao, Y. Cao, and Z. Xie, "Correlation study of biomechanical changes between diabetic eye disease and glaucoma using finite element model of human eye with different iris-lens channel distances," *Med. Eng. Phys.*, vol. 109, 2022, Art. no. 103910.
- [28] Y. Murayama, C. E. Constantinou, and S. Omata, "Development of tactile mapping system for the stiffness characterization of tissue slice using novel tactile sensing technology," *Sensors Actuators A: Phys.*, vol. 120, no. 2, pp. 543–549, 2005.
- [29] K. Shao, J. Zheng, K. Huang, H. Wang, Z. Man, and M. Fu, "Finite-time control of a linear motor positioner using adaptive recursive terminal sliding mode," *IEEE Trans. Ind. Electron.*, vol. 67, no. 8, pp. 6659–6668, Aug. 2020.
- [30] J. Li, X. Xiang, and S. Yang, "Robust adaptive neural network control for dynamic positioning of marine vessels with prescribed performance under model uncertainties and input saturation," *Neurocomputing*, vol. 484, pp. 1–12, 2022.
- [31] Z. Zheng and M. Feroskhan, "Path following of a surface vessel with prescribed performance in the presence of input saturation and external disturbances," *IEEE/ASME Trans. Mechatron.*, vol. 22, no. 6, pp. 2564–2575, Dec. 2017.
- [32] M. Chen, S. S. Ge, and B. Ren, "Adaptive tracking control of uncertain mimo nonlinear systems with input constraints," *Automatica*, vol. 47, no. 3, pp. 452–465, 2011.
- [33] S. S. Ge and C. Wang, "Adaptive neural control of uncertain MIMO nonlinear systems," *IEEE Trans. Neural Netw.*, vol. 15, no. 3, pp. 674–692, May 2004.
- [34] J. W. Kim, P. Zhang, P. Gehlbach, I. Iordachita, and M. Kobilarov, "Deep learning guided autonomous surgery: Guiding small needles into sub-millimeter scale blood vessels," 2023, arXiv:2306.10133.
- [35] D. Arikan et al., "Towards motion compensation in autonomous robotic subretinal injections," 2024, arXiv:2411.18521.
- [36] B. Gonenc, N. Tran, C. N. Riviere, P. Gehlbach, R. H. Taylor, and I. Iordachita, "Force-based puncture detection and active position holding for assisted retinal vein cannulation," in *Proc. 2015 IEEE Int. Conf. Multisensor Fusion Integration Intell. Syst.*, 2015, pp. 322–327.
- [37] A. Alamdar, N. Patel, M. Urias, A. Ebrahimi, P. Gehlbach, and I. Iordachita, "Force and velocity based puncture detection in robot assisted retinal vein cannulation: In-vivo study," *IEEE Trans. Biomed. Eng.*, vol. 69, no. 3, pp. 1123–1132, Mar. 2022.



Bo Hu received the B.E. degree in automation, and the M.S. degree in control science and engineering, from Beijing Technology and Business University, Beijing, China, in 2018, and 2021, respectively. He is currently working toward the Ph.D. degree in control science and engineering, Nankai University, Tianjin, China.

His research interests include micromanipulation and nonlinear control.



Ruimin Li received the B.Eng. degree in intelligence science and technology from the Hebei University of Technology, Tianjin, China, in 2022. She is currently working toward the Ph.D. degree in control science and engineering with Nankai University, Tianjin.

Her research interests include robotic patch clamp system, micromanipulators, and microsystems.



Shiyu Xu received the bachelor's degree in measurement and control technology and instrument from Beijing Jiaotong University, Beijing, China, in 2022. He is currently working toward the master's degree with the College of Artificial Intelligence, Nankai University, Tianjin,

His current research interests include microfluidics and microinjection of ophthalmic drugs.



Rongxin Liu is currently working toward the master's degree from the College of Artificial Intelligence, Nankai University, Tianjin, China.

His current research interests include microinjection modeling and control.



Zengshuo Wang received the B.Eng. degree in automation from the Taiyuan University of Technology, Taiyuan, China, in 2021. He is currently working toward the Ph.D. degree in control science and engineering with Nankai University, Tianiin

His research interests include micromanipulators and medical image analysis.



Mingzhu Sun (Member, IEEE) received the B.S. degree in computer science and technology, the M.S. degree in computer application, and the Ph.D. degree in control theory and control engineering from Nankai University, Tianjin, China, in 2003, 2006, and 2009, respectively.

She is currently a Professor and the Deputy Director of the Institute of Robotics and Automatic Information System. She joined the faculty with Nankai University in 2009 Her research interests include micromanipulation, image pro-

cessing, and computer vision.



Xin Zhao (Member, IEEE) received the B.S. degree from Nankai University, Tianjin, China, in 1991, the M.S. degree from the Shenyang Institute of Automation, CAS, Shenyang, China, in 1994, and the Ph.D. degree from Nankai University in 1997, all in control theory and control engineering.

He joined the faculty with Nankai University in 1997, where he is currently a Professor and the Dean of the College of Artificial Intelligence. His research interests include micromanipula-

tion, microsystems, and mathematical biology.